

Supporting Information for

**Spatial and Temporal Variations in Earthquake Stress Drop on Gofar
Transform Fault, East Pacific Rise: Implications for Fault Strength**

Pamela A. Moyer¹, Margaret S. Boettcher¹, Jeffery J. McGuire², and John A. Collins²

¹Department of Earth Sciences, University of New Hampshire, Durham, NH, USA

²Department of Marine Geology and Geophysics, Woods Hole Oceanographic Institution,
Woods Hole, MA, USA

Contents of this file

Supplemental Text

Figures S1 to S9

Introduction

The supporting information includes descriptions of our corner frequency comparison, seismic moment analysis, V_P/V_S comparison, stress drop with depth, stress drop and P wave velocity reduction linear regression, and 9 Figures with captions.

1. Corner Frequency Comparison

Our approach to modeling spectral ratios results in different sets of corner frequencies that we used for comparison. In Step 1, each spectral ratio was modeled individually yielding one corner frequency from each ratio (Figure S1a). In Step 2, spectral ratios were modeled simultaneously yielding one corner frequency from each EGF (Figure S1b). A third option for comparison is the corner frequency from the model to the stack (average), which yields one corner frequency from each EGF (Figure S1c). We include stacking spectral ratios in our comparison because this is another common approach that may limit variability in the corner frequency due to noise in individual ratios (e.g. Kaneko and Shearer, 2014; Abercrombie et al., 2017). We obtained corner frequencies using each technique with the same data presented in our stress drop study. We followed the same procedure for modeling the stacked spectral ratio as we did for modeling individual spectral ratios in Step 1.

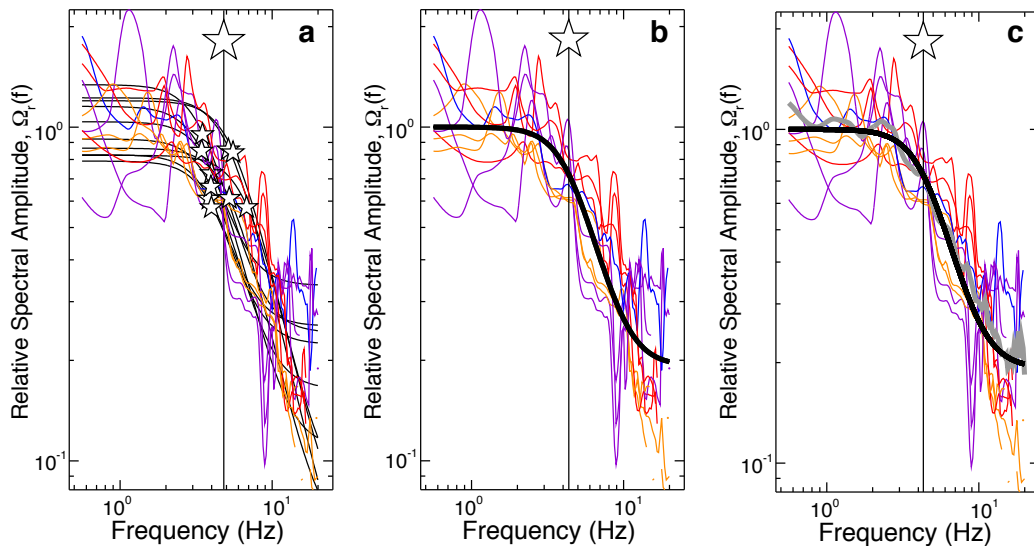


Figure S1. Techniques for obtaining corner frequency (stars) from spectral ratios (colored by station). Models to the ratios are shown in black. (a) A weighted average corner frequency (large star) of 4.8 Hz is obtained from the model to each ratio. (b) A corner frequency of 4.4 Hz is obtained from the simultaneous minimization to all ratios. (c) A corner frequency of 4.3 Hz is obtained from the model to the stack to the ratios (dark gray line).

Although the three techniques produce similar sets of corner frequencies, we observe slight but systematic differences. Corner frequencies found by modeling each spectral ratio (Figure S2, blue curve a) were slightly higher than corner frequencies from simultaneously modeling spectral ratios (Figure S2, black curve b). This is likely because more data is excluded at low frequencies than high frequencies in our study due to signal-to-noise requirements, so the models to each spectral ratio are better constrained at higher frequencies. Corner frequencies found by modeling the stack to the spectral ratio (Figure S2, red curve c) were just slightly lower than corner frequencies from the simultaneous model to the spectral ratios. In this case, the stack artificially gave weight to low frequencies that were missing due to signal-to-noise requirements. We prefer simultaneous modeling (Figure S2, black curve b) over the other techniques because all ratios are included in the minimization at the same time, making the model best constrained at frequencies with the most data.

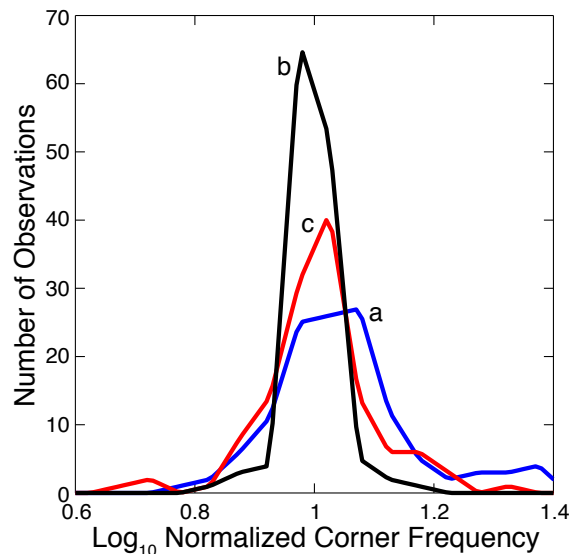


Figure S2. Corner frequencies from the (a) the weighted average to each ratio, (b) the simultaneous model to all ratios (b), and (c) the model to the stack of the ratios. Values from each technique are normalized by the corner frequency from the simultaneous model to all EGFs. The area under the curve indicates the range in corner frequencies from each technique.

We also implemented a bootstrap resampling technique (Efron, 1979) to obtain error estimates on corner frequency to compare with our 5% normalized variance criterion and weighted average technique. This approach allowed us to obtain a nonparametric estimate of the target event corner frequency uncertainty. Details of the bootstrap technique we implemented are provided in the main manuscript and briefly described here. We used corner frequencies from each spectral ratio for each target event (i.e. Figure S1a) and resampled, with replacement, these results 10,000 times. In each sample, we selected the same number of corner frequencies as in the original results. We calculated the mean of each resampled group to obtain a distribution of mean corner frequencies. The target event corner frequency and the error on corner frequency were chosen at the mean value and 95% confidence level of the bootstrap results, respectively. Corner frequency uncertainty using the bootstrap approach was similar to the uncertainty using the 5% normalized variance criterion and weighted average technique (Figure S3), and yielded average error bar lengths of $\log_{10} 0.13$ Hz and $\log_{10} 0.12$ Hz, respectively.

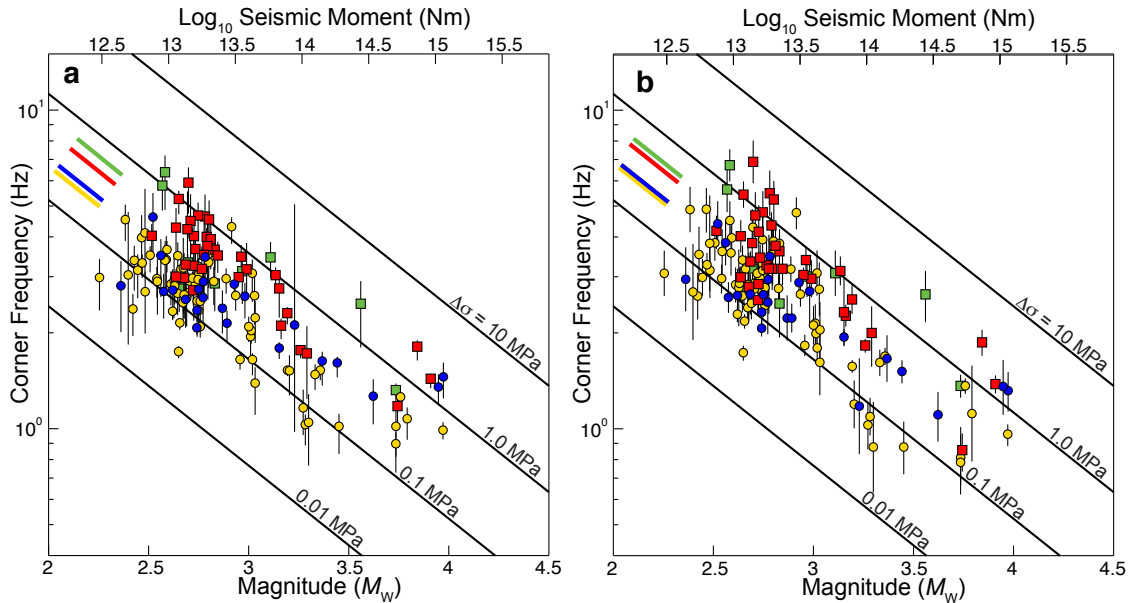


Figure S3. Corner frequency and seismic moment for 138 earthquakes color-coded by position along Gofar. (a) Corner frequency and associated uncertainty determined by bootstrap resampling corner frequencies from individual ratios (Technique 1, Figure S1a). Error estimates on corner frequency were made at the 95% confidence level from the bootstrap results. (b) Corner frequency and associated uncertainty determined by a 5% normalized variance criterion and weighted average technique described in detail in the main manuscript (Technique 2, Figure S1b). Colored-coded bars identify weighted average stress drops within each zone.

2. Seismic Moment Analysis

Seismic moments were obtained from broadband OBS data and the long-period portion of the *S* waves vertical component displacement spectra. We highpass filtered the velocity waveforms at 0.6 Hz to remove low frequency microseisms before integration to displacement. We then windowed the displacement waveforms and used 0.2 s before and 10 s after the *S* wave arrival for spectral analysis (Figure S4a). The windowed waveforms were transformed into the frequency domain (Figure S4b) using the multitaper technique of Prieto et al. (2009) using 7 tapers and a time bandwidth product of 4. We resampled the *S* wave spectrum on a logarithmic axis and excluded signal spectra (Figure S4b, purple curve) at frequencies ≤ 3 times the level of

the noise spectrum (Figure S4b, dashed curve) using pre- S wave arrival waveforms and excluded signal more than 80% of the Nyquist frequency.

Each displacement spectrum was modeled by the far-field displacement spectrum several rupture lengths from the source (Aki, 1967; Brune, 1970), where $\Omega(f)$ is the displacement amplitude spectrum, f is frequency, Ω_0 is the low frequency spectral level, f_c is the corner frequency, t is travel time based on the time difference between the P wave and S wave arrivals, Q is the quality factor, and n and γ control the high frequency fall-off and shape of the corner, respectively:

$$\Omega(f) = \frac{\Omega_0 e^{-\left(\frac{\pi ft}{Q}\right)}}{\left(1 + \left(\frac{f}{f_c}\right)^{2n}\right)^{\frac{1}{\gamma}}} \quad (\text{S1})$$

We used the Boatwright (1980) model with $\gamma = 2$ and a constant Q of 150 for S waves based on a velocity model through the foreshock zone of Gofar from Roland et al. (2012). The residual between the Boatwright (1980) model (Figure S4b, black curve) and the displacement spectrum (Figure S4b, purple curve) was minimized using the Nelder-Mead least squares optimization technique. The free parameters in the optimization were Ω_0 and f_c ; initialized to the mean spectral amplitude and mean frequency, respectively.

We obtained a measure of uncertainty on the low frequency spectral level by remodeling the displacement spectrum with a range of values between $\log_{10}(\Omega_0) - 0.75$ and $\log_{10}(\Omega_0) + 0.75$ in 0.05 units from the best fit value and using corner frequency as a free parameter (Figure S4c and S4d). The high and low error limits on Ω_0 were chosen where the normalized variance was 5% of the best fit value, and we excluded spectra with normalized variance that did not exceed 5% of the minimum variance. While we obtained a value for corner frequency from the model to

the displacement spectrum, it is poorly constrained without the removal of path effects and not used for analysis.

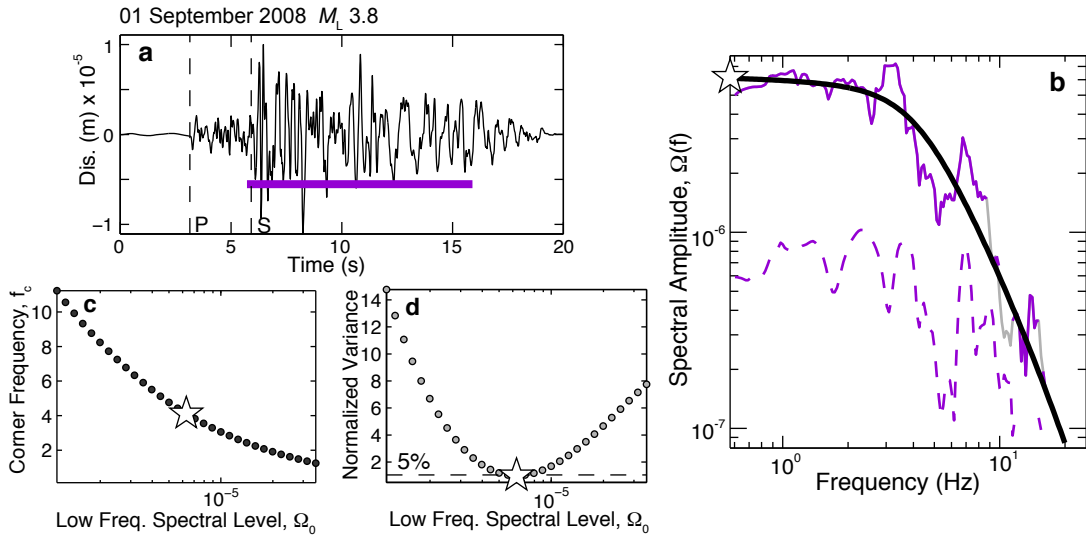


Figure S4. (a) Vertical component displacement waveform used to obtain seismic moment. A thick horizontal line highlights the waveform used for analysis. (b) S wave displacement spectrum (solid purple line) and pre-event noise spectrum (dashed purple line). Signal that was excluded from analysis or did not meet our signal-to-noise criterion are shown in gray (above ~ 9 Hz). The displacement spectrum was modeled by equation (S1) (black line) with Ω_0 , and f_c as free parameters. The low frequency spectral level from the model with minimum variance is shown as a star. (c) The displacement spectrum was remodeled with f_c as a free parameter for fixed values of Ω_0 . (d) The normalized variance between the spectral data and model for each model tested. We used a high and low error estimate on Ω_0 at 5% normalized variance (dashed line).

Next, we simultaneously modeled the displacement spectra from each station using equation (S1) (Figure S5). To perform the simultaneous model, we updated spectral amplitudes to moment rate spectra following Brune (1970), and multiplied each displacement spectrum by $4\pi\rho\beta^3 R\Omega(f) / FU_s$, where ρ is crustal density, R is the hypocentral distance between the station and event, $F = 2$ is the free surface parameter, and $U_s = 0.63$ is the mean radiation pattern for S waves (Aki & Richards, 1980). Based on the velocity model of Roland et al. (2012), we used $\rho = 2,900 \text{ kg/m}^3$ and $\beta = 3,400 \text{ m/s}$. We again optimized the least-squares solution to obtain a

model that minimized the residual between the moment rate spectra and model to obtain seismic moment. We used the same initial parameters for the simultaneous minimization as we did for modeling individual displacement spectra, and remodeled the moment rate spectra to obtain high and low error limits on seismic moment where the normalized variance is 5% of the best fit value (Figure S5d). To retain azimuthal variation, we only used seismic moments that had moment rate spectra from at least three stations.

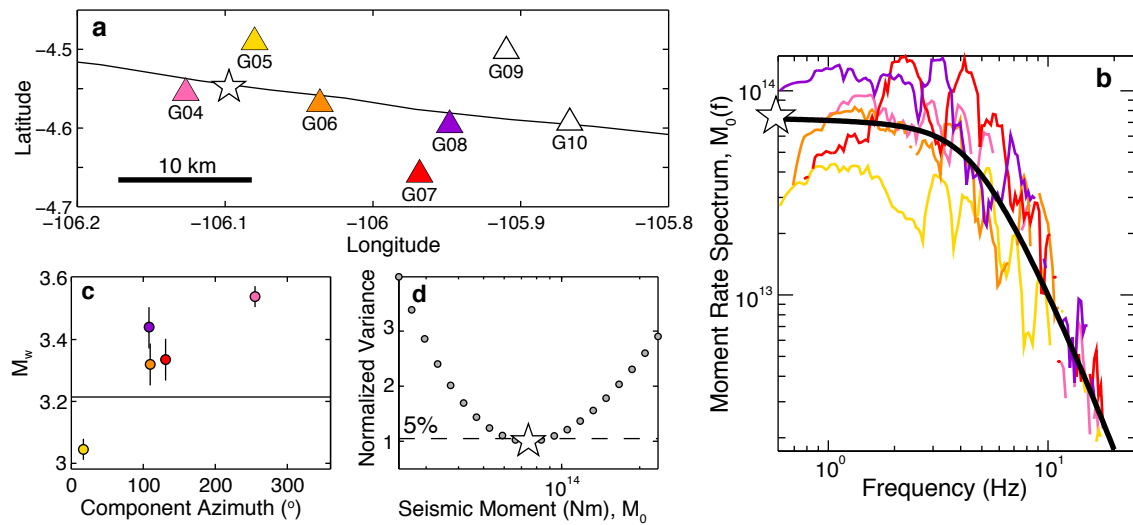


Figure S5. (a) Location of the earthquake (star) with moment rate spectra shown in b. (b) Spectra are color-coded by station and modeled by the simultaneous minimization (black line). The low frequency level from the model corresponding to the seismic moment with minimum variance is shown at 7.44×10^{13} Nm (star). (c) Magnitude from moment rate spectra as a function of azimuth. The horizontal line is the magnitude from the best fit model. (d) The variance between spectral data and the model. We used high and low error estimates on the seismic moment at 5% normalized variance (dashed line).

We used the relative surface wave magnitude method of McGuire (2008) to obtain magnitudes for $M_L \geq 4.0$ earthquakes to compare with our spectrally derived values. We used OBS data for large ($M_L \geq 4.0$) earthquakes on Gofar that were also recorded on the nearby Discovery Transform Fault. Four $M_w \geq 5.0$ earthquakes with magnitudes in the Global Centroid Moment Tensor (CMT) catalog were used as reference events. Vertical component waveforms

for reference events and $M_L \geq 4.0$ target events were bandpass filtered between 0.04 and 0.06 Hz (Figure S6) to highlight the long-period (~ 20 s) surface waves. The mean difference in amplitude between waveforms with a cross-correlation coefficient ≥ 0.9 at three or more stations was used to reflect the mean difference in seismic moment between the events. Very good agreement between spectrally derived and surface wave derived magnitudes for $\sim M_W 4.0$ events further suggests that our seismic moment estimates from both methods are robust.

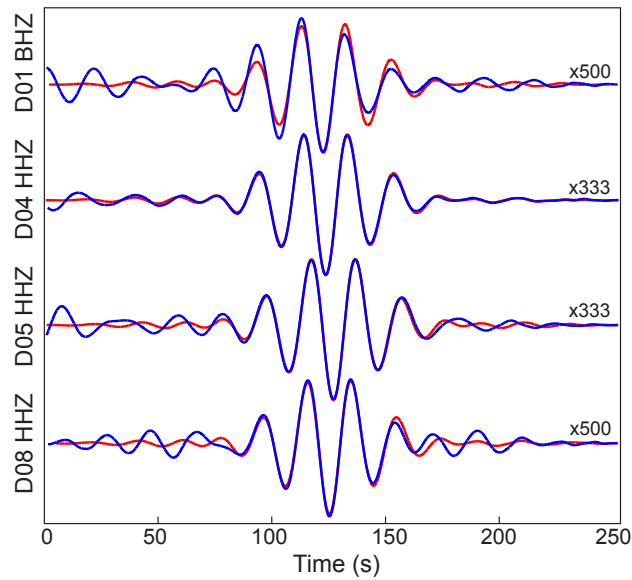


Figure S6. Example of the relative surface wave differential amplitude method (McGuire, 2008) for obtaining magnitude. Waveforms from one accelerometer (BHZ) and four broadband (HHZ) OBSs on Discovery were bandpass filtered between 0.04 and 0.6 Hz. The difference in amplitude between the $M_L 4.3$ target event (blue) and $M_W 6.0$ reference event (red) is noted above each waveform pair.

3. V_P/V_S Comparison

Work by Guo et al. (2018) suggests that V_P/V_S in the foreshock swarm zone may be larger than V_P/V_S in the 2008 rupture asperity. This change would affect our stress drops, which were determined using the same V_P/V_S in all areas of the fault. Without well constrained tomography models for V_S at Gofar, we estimated V_S with an increased V_P/V_S using the P wave velocity

model of Froment et al. (2014). In the foreshock swarm zone at 5-km depth, Froment et al. (2014) found $V_p = 5,590$ m/s. We tested a 20% increase in V_p/V_s to a value of 2.0 in swarm zones, which yielded $V_s = 2,790$ m/s. We checked along-strike variations in stress drop using $V_s = 2,790$ m/s (from $V_p/V_s = 2.0$) in zones of low seismic coupling, and $V_s = 3,400$ m/s (from $V_p/V_s = 1.73$) in zones of high seismic coupling. With spatially varying V_s , stress drops in swarm zones increased and the difference in weighted average values between zones of high and low seismic coupling was reduced (Figure S7). However, we still found significant variation between swarm zone and rupture asperity stress drops at the 99% confidence level using both the Student's t -test and the permutation test (Efron and Tibshirani, 1993) at 10,000 iterations. V_p/V_s in swarms zones would have to increase by 85% (to a value of 3.2) compared to V_p/V_s in rupture asperities before the difference in stress drops in zones of high and low seismic coupling were no longer statistically significant at the 99% confidence level. A high $V_p/V_s = 3.2$ on Gofar is also inconsistent with the results of McGuire et al. (2012), who found little difference between V_p/V_s in the lower crust of the foreshock swarm zone and 2008 rupture asperity (1.67 and 1.73, respectively).

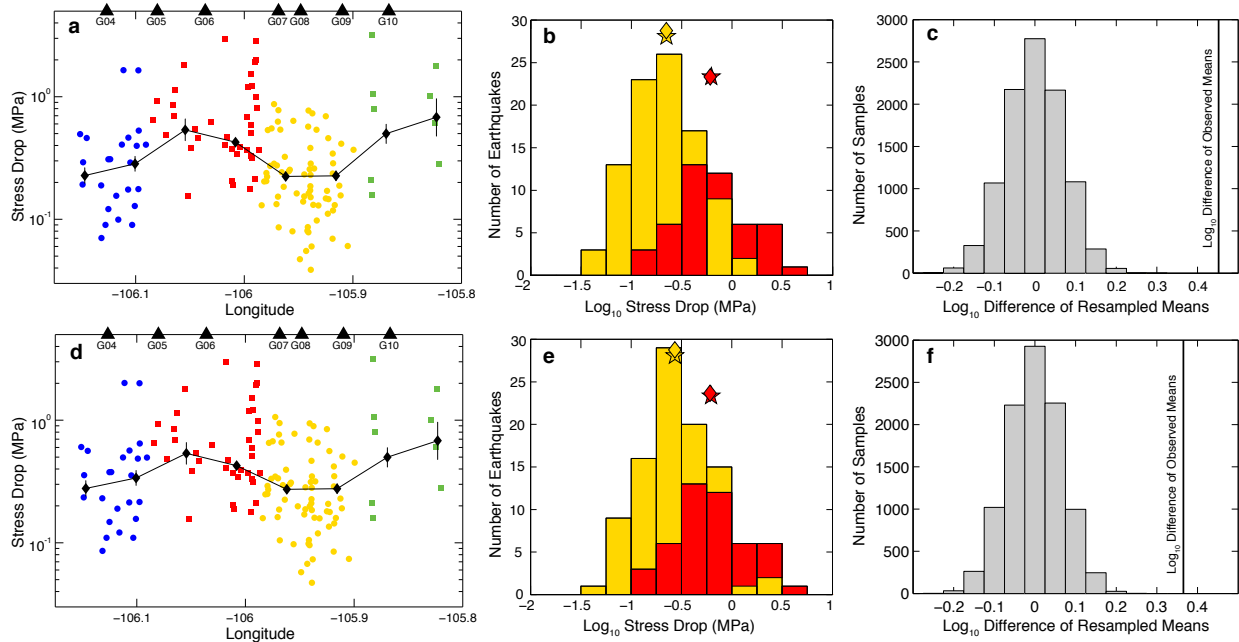


Figure S7. (a) Stress drops for earthquakes in zones of high (green and red squares) and low (yellow and blue circles) seismic coupling using the same V_p/V_s in all areas of the fault. (b) Distribution of stress drops for earthquakes in zones of high (red) and low (yellow) seismic coupling using the same V_p/V_s in all areas of the fault. Mean and median stress drops are noted by stars and diamonds, respectively. (c) Distribution of the difference of the means for resampled stress drops, and the difference of the mean of the observed stress drops (vertical line) from a and b. (d-f) Same as a, b, and c except we used a V_p/V_s in the swarm zones that was 20% higher than the V_p/V_s in the rupture asperities.

4. Stress Drop with Depth

We compared our stress drops with depths from the double-difference catalog of Froment et al. (2014), but did not resolve any depth dependence on stress drop (Figure S8). Weighted average stress drops are relatively constant within our 3-10 km depth range. Earthquakes in the foreshock swarm extended deeper than the aftershocks (McGuire et al., 2012; Froment et al., 2014), but we found no statistically significant increase in stress drop with depth in the foreshock and December swarm zones.

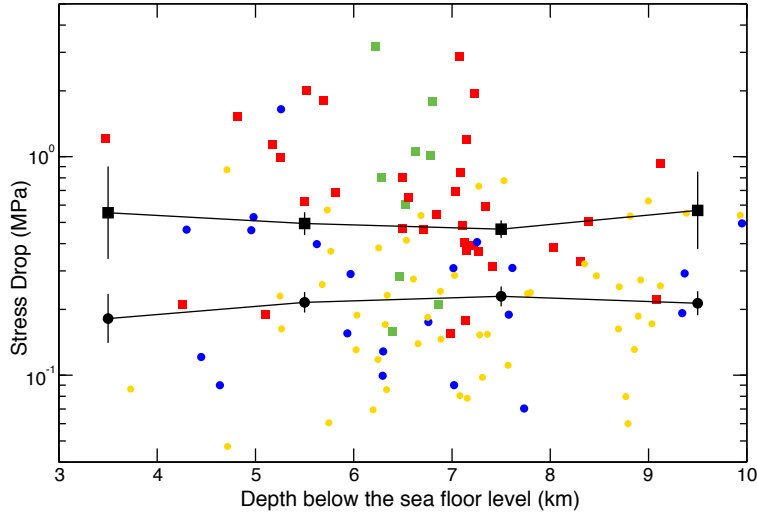


Figure S8. Stress drops as a function of depth for earthquakes in zones of high (green and red squares) and low (yellow and blue circles) seismic coupling. A line connects weighted average values in 2-km bins from each zone and shows no significant variation in stress drop with depth.

5. Stress Drop and *P* Wave Velocity Reduction Linear Regression

We compared our stress drops before the M_W 6.0 mainshock in the foreshock swarm zone and 2008 rupture asperity to the *P* wave seismic velocity structure of Froment et al. (2014). We focused on pre-mainshock stress drops and found lower stress drops in the foreshock swarm zone where enhanced fluid circulation in highly-fractured fault material is inferred (Roland et al., 2012; Froment et al., 2014) compared to the rupture asperity. An inverse relationship between stress drop and *P* wave velocity reduction is highlighted with a least-squares linear regression using a first order polynomial (main manuscript, Figure 11, solid gray line). We tested the statistical significance of a regression model with negative slope to the data compared to a least squares best fit horizontal line (main manuscript, Figure 11, dashed line) using the Levene test (Levene, 1960). We computed the residuals to the regression models (Figure S9), and tested the likelihood that the variance between the data and a horizontal line (our null hypothesis) came from the same population as the variance between the data and a linear model with negative slope. We obtained a probability for equal variances of 0.1, and rejected the null hypothesis at

the 90% confidence level; finding the line with negative slope a statistically significant interpretation of the relationship between stress drop and damage.

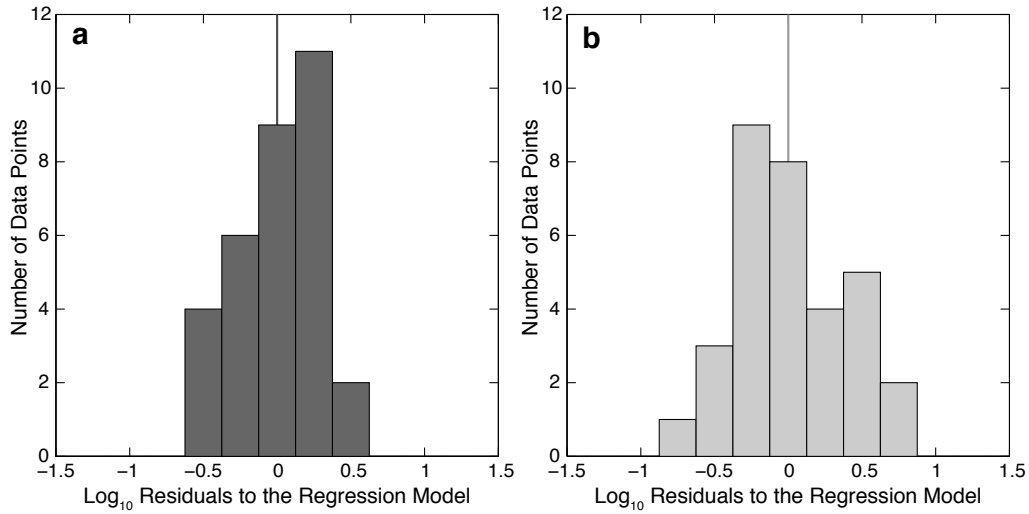


Figure S9. (a) Distribution of residuals between the data and a first-order polynomial with negative slope. The variance of the residuals to this regression model is 0.08. (b) Distribution of residuals between the data and a horizontal line representing the null hypothesis. The variance of the residuals to this regression model is 0.14. The mean of the residuals from each distribution is identified by a vertical line.

References

- Abercrombie, R. E., Bannister, S., Ristau, J., & Doser, D. (2017). Variability of earthquake stress drop in a subduction setting, the Hikurangi Margin, New Zealand. *Geophysical Journal International*, 208(1), 306-320. <https://doi.org/10.1093/gji/ggw393>
- Aki, K. (1967). Scaling law of seismic spectrum. *Journal of Geophysical Research*, 72, <https://doi.org/10.1029/JZ072i004p01217>
- Aki, K., & Richards, P. G. (1980). Quantitative seismology: Theory and methods. San Francisco: W. H. Freeman
- Boatwright, J. (1980). A spectral theory for circular seismic sources: Simple estimates of source dimension, dynamic stress drop, and radiated seismic energy. *Bulletin of the Seismological Society of America*, 70, 1-28
- Brune, J., (1970). Tectonic stress and the spectra of seismic shear waves from earthquakes. *Journal of Geophysical Research*, 75, 4997-5009
- Efron, B. (1979). Bootstrap methods: Another look at the jackknife, *Annals of Statistics*, 7(1), 1-26. <https://doi.org/10.1214/aos/1176344552>
- Efron, B., & Tibshirani, R. J. (1993). An Introduction to the Bootstrap, Monographs on Statistics and Applied Probability. New York: Chapman and Hall
- Froment, B., McGuire, J. J., van der Hilst, R. D., Gouedard, P., Roland, E. C., Zhang, H., & Collins, J. A. (2014). Imaging along-strike variations in mechanical properties of the Gofar transform fault, East Pacific Rise. *Journal of Geophysical Research*, 119, 7175-7194. <https://doi.org/10.1002/2014JB011270>
- Guo, H., Zhang H., & Froment, B. (2018). Structural control on earthquake behaviors revealed by high-resolution V_p/V_s imaging along the Gofar transform fault, East Pacific Rise.

- Earth and Planetary Science Letters, 499, 243-255.
<https://doi.org/10.1016/j.epsl.2018.07.037>
- Kaneko, Y., & Shearer, P. M. (2014). Seismic source spectra and estimated stress drop derived from cohesive-zone models of circular subshear rupture. *Geophysical Journal International*, 197, 1002-1015. <https://doi.org/10.1093/gji/ggu030>
- Levene, H. (1960). Robust Tests for Equality of Variances. In I. Olkin et al. (Eds.), *Contributions to Probability and Statistics: Essays in Honor of Harold Hotelling* (pp. 278-292). Stanford University Press, Palo Alto, CA
- McGuire, J. J. (2008). Seismic cycles and earthquake predictability on East Pacific Rise transform faults. *Bulletin of the Seismological Society of America*, 98, 1067-1084.
<https://doi.org/10.1785/0120070154>
- McGuire, J. J., Collins, J. A., Gouedard, P., Roland, E., Lizarralde, D., Boettcher, M. S., Behn, M. D., & van der Hilst, R. D. (2012). Variations in earthquake rupture properties along the Gofar transform fault, East Pacific Rise. *Nature Geoscience*, 5(5), 336-341.
<https://doi.org/10.1038/ngeo1454>
- Prieto, G. A., Parker, R. L., & Vernon III, F. L. (2009). A Fortran 90 library for multitaper spectrum analysis. *Computers & Geosciences*, 35, 1701-1710.
<https://doi.org/10.1016/j.cageo.2008.06.007>
- Roland, E. (2012). Earthquake Behavior and Structure of Oceanic Transform Faults, (Doctoral dissertation). Retrieved from (<https://dspace.mit.edu/handle/1721.1/70778>). Cambridge, MA: Massachusetts Institute of Technology